14th International Symposium on Turbulence and Shear Flow Phenomena (TSFP14)
Heidelberg, Germany, July 28–31, 2026

TOWARDS RESOLVING TURBULENT TWO-PHASE BOUNDARY LAYERS IN AIR LUBRICATION BY MULTIBEAM SONAR TECHNOLOGY

Malte Skyberg, Claes Poulsen, Pourya Forooghi, Ulrich Doll
Department of Mechanical and Production Engineering
Aarhus University
Katrinebjergvej 89 G-F, 8200 Aarhus N
ud@mpe.au.dk

ABSTRACT

Air lubrication is a promising technology to reduce ship fuel consumption and CO_2 emissions, but its effectiveness depends on bubble size, distribution, and persistence in the turbulent near-wall boundary layer. Measuring these parameters at full scale remains a major challenge. This work evaluates ultrasonic multibeam sonar as a non-intrusive diagnostic for the characterization of air lubrication layers. Laboratory experiments with controlled bubble injection were used to compare sonar measurements with synchronized optical imaging. Richardson–Lucy deconvolution improved the localization of both sparse and dense bubble plumes and increased agreement with optically observed bubble-rich regions. However, accurate bubble sizing was not achieved, particularly near the system resolution limit of approximately 8 mm. The sonar data should therefore be interpreted mainly in terms of bubble position, plume extent, and relative concentration rather than exact bubble diameter, while still highlighting the method's potential for future full-scale deployment in operating air-lubrication systems.

INTRODUCTION

Reducing hydrodynamic drag is crucial for lowering fuel consumption and CO_2 emissions in maritime transport. Air lubrication, which involves injecting air beneath a ship's hull to modify the turbulent boundary layer, has shown particular promise; current installations report at least 5% to 16% savings in fuel and CO_2 emissions (Kim & Steen, 2023), with potential for further improvements if the physical mechanisms can be better understood and optimized. The effectiveness of air lubrication depends on how the injected air interacts with the turbulent boundary layer, altering near-wall turbulence and reducing wall shear stress. However, translating laboratory insights to real-world deployment remains technically challenging due to high flow velocities, elevated hydrostatic pressures, limited access beneath operating vessels, and often turbid water conditions. These factors complicate both the implementation and the in-situ measurement of multiphase turbulent interactions, posing significant barriers to optimization at full scale.

As summarized in the review article of Murai (2014), three regimes of air lubrication can be distinguished: bubble drag reduction (BDR), where dispersed bubbles interact with near-wall turbulence; gas layer drag reduction (GLDR), involving a continuous air film that reduces water–solid shear; and gas cavity drag reduction (GCDR), where large air cavities persist under the hull. Murai concludes that substantial drag-reduction gains are possible for favorable combinations of bubble size and flow speed, whereas unfavorable conditions may lead to only minor improvements or even negative effects. This highlights the importance of both bubble size and spatial distribution within the boundary layer. Equally important is the persistence of air within the near-wall region, where its influence on drag reduction is greatest. Air that migrates away from this inner boundary-layer region contributes less effectively to lubrication and may therefore represent wasted injection energy.

Drag reduction by air lubrication has been investigated through a range of experimental approaches, with laboratory studies employing high-resolution optical methods such as high-speed imaging and particle image velocimetry to track bubble distributions and air layer persistence, as well as direct drag measurements using calibrated load cells and dynamometers (Elbing *et al.*, 2008; Ceccio, 2010; Kitagawa *et al.*, 2019; Kringel *et al.*, 2025). Most experiments that achieve local resolution of bubble–turbulence interactions have been conducted in laboratory channels and towing tanks, where the controlled environment enables detailed study of bubble size, distribution, and their effects on turbulent boundary layers (Elbing *et al.*, 2008, 2013; Mäkiharju *et al.*, 2017; Kitagawa *et al.*, 2019; Tanaka *et al.*, 2022; Zhang *et al.*, 2021; Tanaka *et al.*, 2023). In contrast, full-scale deployments on operational vessels typically rely on indirect performance metrics such as engine power consumption and fuel usage to assess drag reduction (Mizokami *et al.*, 2010; Kumagai *et al.*, 2015; Kim & Steen, 2023). While these measurements provide essential validation, the actual drag reduction mechanism at full scale remains uncertain due to a lack of high resolution measurement techniques suitable for deployment on operating vessels.

Due to the large acoustic impedance difference of nearly four orders of magnitude between air and water, ultrasound-based sensing emerges as a viable option for high-resolution studies of air lubrication layers. This pronounced mismatch results in a reflection coefficient close to unity at the air–water interface, producing strong backscatter signals even from submillimeter bubbles (Murai *et al.*, 2010).

Considering the challenges of full-scale deployment, sonar systems specifically developed for harsh maritime environments offer a promising alternative. For instance, Veloso *et al.* (2015) used a low-frequency single-beam sonar system to identify and quantify gas leaks on the seafloor, while Zhang *et al.* (2022) demonstrated the use of an ultrasonic multibeam sonar to resolve bubble plumes with high spatial detail. Compared to single-beam systems, multibeam sonar arrays provide significantly enhanced spatial coverage and angular resolution, enabling more accurate characterization of bubble distributions. Their ability to operate in turbid, sediment-rich waters and withstand high pressures and hydrodynamic loads makes them particularly suited for deployment beneath operating vessels.

This work constitutes a first step toward qualifying high-frequency multibeam imaging sonar for the spatial characterization of air lubrication layers. The objective of this study is determine whether a calibrated image-level deconvolution framework can improve the recovery of bubble-plume structure, location, and boundaries. Validation is performed using synchronized optical recordings, while the present limits of quantitative size interpretation are discussed explicitly.

METHODOLOGY

Two separate methodologies were applied to evaluate bubble region characterization using optical imaging and ultrasonic multibeam sonar measurements. The optical method provides a reference for bubble edge detection under controlled laboratory conditions, while the sonar-based method aims to extract equivalent cluster information from acoustically resolved bubble regions.

Experimental Setup

Figure 1 shows the laboratory setup used for the experiments. The tests were conducted in a tank measuring 10 m in length, 2 m in width, and with a water depth of 1.5 m. A Kongsberg Flexview multibeam sonar operating at 1400 kHz, with a horizontal field of view of 46°, was used for the acoustic measurements. The sonar was mounted vertically with an upward tilt of 23°, positioned 2 cm above the tank floor in order to minimize backscatter from the bottom and side wall. Air bubbles were generated 0.8 m from the sonar using a compressor system connected to interchangeable nozzles, allowing control of injection rate, plume density, and characteristic bubble size. The nozzle types included perforated tubes with different hole diameters as well as porous oxygen stones. For independent optical validation, a Basler ACE 2 camera equipped with a 25 mm lens and a green filter was aligned with the sonar field of view. The optical measurements were acquired by pulsed green back-illumination using an Advanced Illumination SL316 light source to obtain sharp bubble contours. The effective exposure time was determined by the strobe pulse duration of 1500 μs. Calibration spheres were placed in the field of view prior to each run to establish the pixel-to-millimeter conversion factor and spatial calibration between sonar and camera. Sonar and camera data were recorded simultaneously under quiescent water conditions. For synchronization, the sonar acted as the master at a ping rate of 15 Hz, while the camera and light source were configured as slaves.

Image Data Analysis

Bubble boundaries from the optical images were determined using a custom MATLAB-based image-analysis routine. The image scale was first calibrated using calibration spheres placed in the measurement plane. After manually indicating the approximate sphere locations, each sphere was segmented automatically, and its equivalent diameter in pixels was determined.

To reduce the influence of non-uniform illumination, a mean background image was constructed from a set of background frames. Each bubble image was then processed relative to this background using both a normalized intensity-ratio image and a background-difference image. Bubble candidates were identified by combining several complementary image features: a dark bubble core, nearby rim edges, and bright regions associated with the illuminated bubble boundary. These features were merged into a binary mask and refined using morphological operations and object-selection criteria to obtain the final bubble contours. Only detections inside a predefined analysis ROI were analysed, and detections too close to the ROI boundary were excluded to avoid poorly illuminated edge regions of the field of view. For each detected bubble, the projected area was outlined and converted to a boundary map, which can be overlayed onto the sonar image. An example of the bubble contours obtained from the image-processing routine is shown in Figure 2.

High-Frequency Multibeam Imaging Sonar

The objective of the sonar-based methodology is to extract the maximum physically meaningful information on bubble-plume structure and spatial distribution from the available measurements. Achieving this requires an understanding of both the underlying acoustic measurement principle and the limitations associated with commercially available imaging sonar hardware.

The high-frequency multibeam echo sounder (HF-

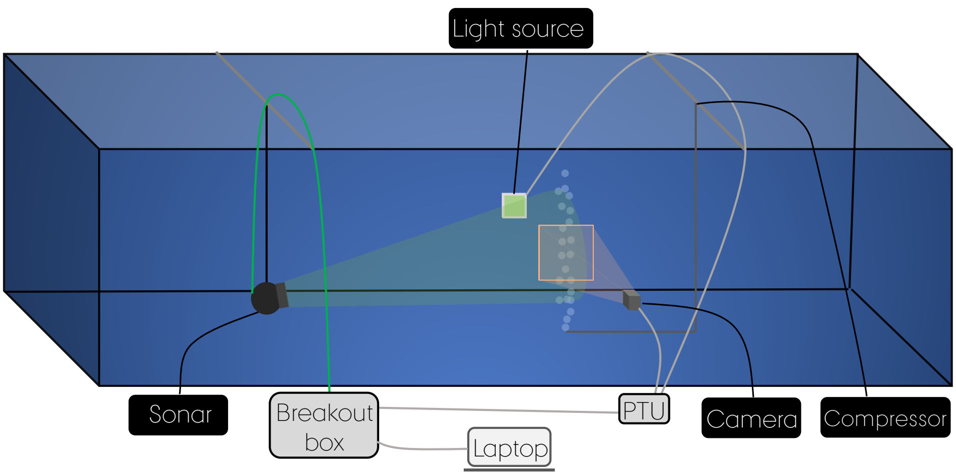

Figure 1: Schematic of the experimental setup.

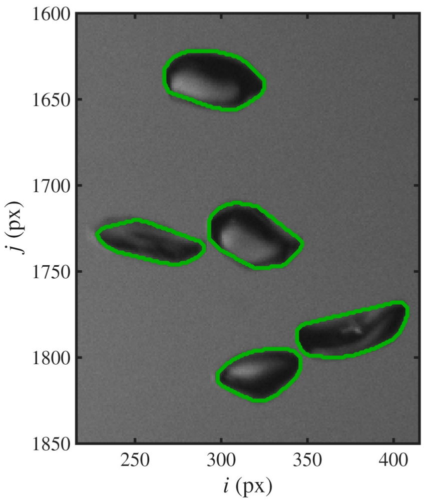

Figure 2: Example of bubble contours extracted from the optical images using the MATLAB image-processing routine.

MBES) employed in this study belongs to the class of imaging sonar systems. Imaging sonars are designed for two-dimensional spatial imaging and offer high angular resolution together with wide spatial coverage in a compact form. In the present application, this makes multibeam sonar well suited for resolving the spatial boundary, position, and structure of the bubble plume.

The sonar used consists of a single acoustic transmitter and a linear array of receiver elements. For each ping, a narrowband acoustic pulse is transmitted, and the backscattered acoustic pressure field is recorded as a function of time by each receiver element. These pressure fluctuations are converted into electrical voltage signals, which constitute the raw time-domain measurements prior to beamforming. The beamforming process then combines the time-delayed receiver signals to produce a two-dimensional image in range and angle.

For the present study, the lack of absolute acoustic calibration is addressed by focusing on relative intensity patterns and spatial signatures of bubble backscatter rather than on absolute scattering cross-sections. This is consistent with the primary objective of the work, namely to resolve the spatial organization of bubbly structures within the near-wall region of an air-lubrication layer, where spatial resolution and robustness are of greater importance than absolute acoustic quantification.

Beamforming And Image Construction

In most commercial HF-MBES instruments, access to these raw channel-level data is restricted, and the beamforming process is implemented internally using proprietary algorithms. For the present study, partial access to the beamforming workflow was obtained through a processing script provided by manufacturer. This allowed several beamforming-related settings to be controlled, although the full beamformer implementation remained inaccessible.

To form the sonar images, the full set of receiver elements was used and the manufacturer's receiver-specific correction factors was applied before beamforming. Beamforming in the azimuth direction was turned on, while leaving the range direction without additional weighting by not applying additional Kaiser filtering. These choices were made to avoid extra smoothing or reshaping of the measured signal during calibration, so that the calibration would reflect the sonar system's standard imaging behavior as closely as possible.

The resulting sonar image should therefore be understood as the output of the full commercial sonar system, influenced by the receiver array, the controllable beamforming settings, and internal processing that is not fully accessible.

The beamformed sonar images produced by the used beamformer inherently exhibit a finite point spread function (PSF), which governs the system's spatial resolution. As a result, a single compact acoustic scatterer, such as an isolated calibration sphere seen in Figure 3, does not appear as a point-like feature but rather as an extended intensity pattern characterized by a main lobe and pronounced sidelobes. These sidelobes arise from the finite aperture of the receiver array effecting the point spread cross azimuth, the limited bandwidth of the transmitted pulse that affects the point spread cross range. In dense bubble plumes, the superposition of sidelobes from multiple scatterers leads to elevated background levels and reduced contrast, complicating the direct interpretation of raw sonar images. This overall system response is accounted for through background noise removal, PSF calibration, and subsequent image-level deconvolution, which are described in the following section.

Deconvolution

Because the beamformed image exhibit the systems PSF, further refinements in spatial resolution and noise suppression must be applied at the image level. The following section is based on the work from (Liu *et al.* (2021)). The beamformed sonar image is expressed in the native sonar coordinates, where r denotes the range from the sonar and θ denotes the azimuth angle . The measured image intensity can be interpreted as the convolution I of the true acoustic reflectivity field s with the system's PSF h, contaminated by noise n.

$$I(\theta, r) = h(\theta|r) \cdot \mathbf{s}(\theta, r) + n(\theta, r), \tag{1}$$

Deconvolution aims to invert this process, thereby suppressing sidelobes, sharpening target signatures, and recovering a more faithful representation of the underlying bubble distribution. By knowing or approximating the PSF of the system,

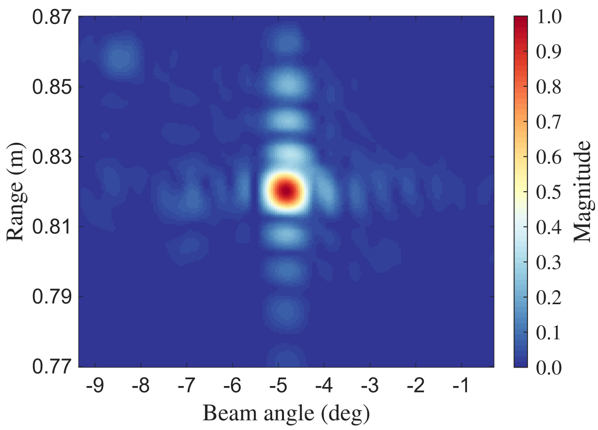

Figure 3: Normalized sonar image of a 9 mm calibration target after background removal. Image showing strong sidelobes caused by the PSF

it becomes possible to apply deconvolution without detailed knowledge of the proprietary beamforming implementation. The PSF is assumed separable in range and angular dimensions:

$$h(r,\theta) \approx h_r(r)\, h_\theta(\theta), \tag{2}$$

where $h_r(r)$ represents the range PSF associated with the transmitted pulse shape and matched filtering, and $h_\theta(\theta)$ represents the angular PSF governed primarily by the receive array geometry and beamforming process. Following the same study, assuming a band-limited transmitted signal with receive bandwidth $B_{\rm rx}$, the range PSF can be expressed as

$$h_r(r) \propto T_{\rm p}\, \mathrm{sinc}\left(\frac{2B_{\rm rx}}{c}\, r\right), \tag{3}$$

where c is the speed of sound in water. The factor T_p is omitted here because it only changes the overall scaling, not the shape of the range PSF. The angular PSF is approximated by the array response function of a uniformly spaced receive aperture, given by

$$h_\theta(\theta) \propto \left| \frac{\sin(\beta N k d 2 \sin\theta)}{\sin(k d 2 \sin\theta)} \right|^2, \tag{4}$$

where N is the known number of receiver elements, d is the element spacing, $k = 2\pi/\lambda$ is the acoustic wavenumber, and β is a dimensionless calibration parameter. The resulting expression retains the main-lobe and sidelobe structure characteristic of conventional delay-and-sum beamforming.

The introduction of β is motivated by the fact that the original expression is based on a far-field approximation of the system PSF. For the present sonar system, this assumption is valid only beyond a range of approximately 17 m, whereas the measurements in this study are primarily conducted in the near- and mid-field. In this region, the PSF deviates from the simplified far-field model and becomes position-dependent (Mei *et al.*, 2020). Although more complete near-field models exist, they are difficult to apply in practice because of their computational cost and sensitivity to modeling errors. Preliminary attempts to implement near-field PSF-based deconvolution based on Goodman (2005) were found to be numerically unstable. Since recent work by Wang *et al.* (2026) has shown that the simpler far-field PSF formulation can still perform well at close range, that approach is adopted here.

The parameter β is therefore used as a practical calibration factor to account for differences between the ideal far-field model and the measured system response, including hardware and processing effects. The calibrated PSF should thus be understood as an empirical approximation of the actual system response. Consequently, the deconvolved image does not represent the true acoustic reflectivity field directly, but rather an improved approximation that reduces sidelobe artifacts and enhances spatial resolution relative to the original beamformed image.

The actual deconvolution is implemented using the Richardson–Lucy (R–L) algorithm due to its robustness and suitability for acoustic imaging (Liu *et al.*, 2021; Huang *et al.*, 2018; Li *et al.*, 2025). It is an iterative method that assumes Poisson-like noise and enforces non-negative solutions. The algorithm starts from the measured image and iteratively refines an estimate of the true reflectivity field. At each step, the current estimate is compared to the measured image after convolution with the updated PSF. The number of iterations controls the trade-off between resolution improvement and noise amplification. In this work, the number of iterations was fixed at 10 to ensure stable results while avoiding over-enhancement.

The calibration of β was performed using steel spheres with known diameters (5.5 mm, 9 mm, and 15 mm). The parameter was adjusted by matching the width of the main lobe (root-to-root) of the observed sonar response to the expected target size. The 15 mm calibration sphere was used as the reference above the manufacturer specified resolution limit of approximately 8 mm. As targets approach this limit, the measured signal becomes increasingly dominated by the system PSF rather than the true object size. The results in Figures 4 show reduced sidelobes and a narrower main lobe in both range and azimuth directions, indicating that the adopted PSF provides a reasonable approximation of the system response.

The calibration tests showed that the smaller spheres

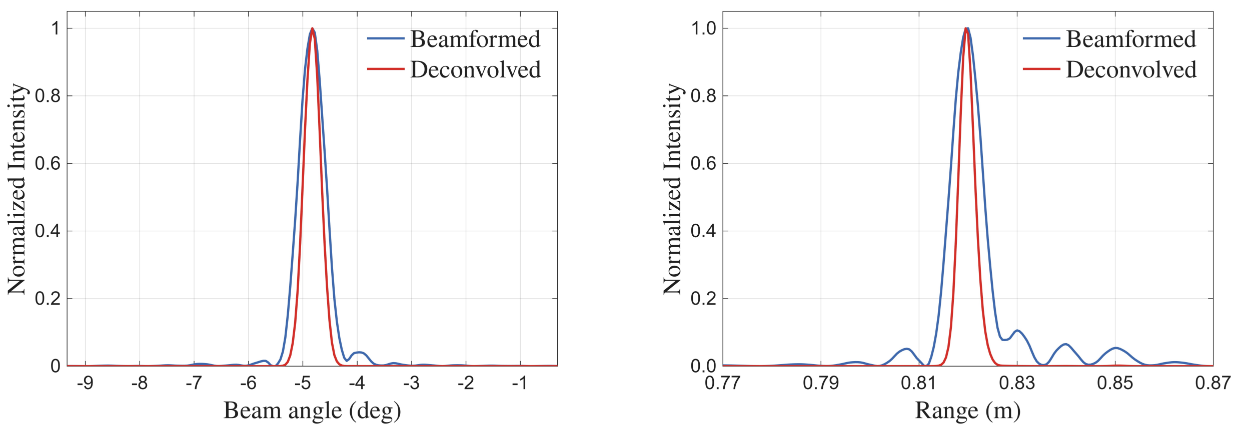

Figure 4: Before and after Richardson–Lucy deconvolution of a calibration sphere of 9 mm. The left panel shows the cross-beam angle intensity profile, and the right panel shows the range intensity profile.

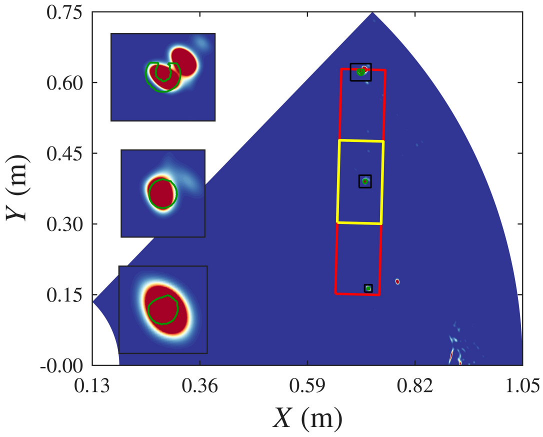

Figure 5: Spatial camera-to-sonar calibration in Cartesian sonar coordinates. The projected camera frame is shown in red and the analysis ROI in yellow. The inset shows the local agreement between the calibration contour and the sonar image around the central 15 mm sphere. The second target is a reflection and was not used.

(5.5 mm and 9 mm) could not be reconstructed accurately at the measurement distance of 0.8 m, as shown in Figure 5. In particular, although the 9 mm sphere appears visually similar in size in the sonar and camera images, the sonar-based diameter estimate is still a few millimetres too large. This limitation is also evident from the fact that the 5.5 mm and 9 mm spheres appear nearly identical in size in the sonar image, indicating that both targets lie under the practical resolution limit.

RESULTS AND DISCUSSION

To evaluate the proposed processing approach, two bubble-plume cases were considered: a sparse bubbles and a denser plume. These cases were used to assess the accuracy of the camera-to-sonar synchronization and alignment, as well as to examine the effect of Richardson–Lucy deconvolution on the acoustic image.

Figure 6 shows the sparse bubble plume, where the optical bubble outlines are overlaid on the sonar image. The mapped contours show good overall spatial correspondence with the dominant acoustic response region, demonstrating that the temporal synchronization and geometric camera-to-sonar registration were sufficiently accurate for image-level comparison. A slight but systematic spatial shift between the camera-derived contours and the sonar response is nevertheless observed. This offset may partly reflect uncertainty in the calibration-based coordinate mapping and time synchronization, but it is also likely influenced by the fact that the bubbles are smaller than the practical resolution limit of the sonar. Thus, the acoustic image reflects a broadened scattering response rather than the true visible boundary, so the comparison should be interpreted as a qualitative validation of bubble position rather than exact contour overlap.

The sparse plume case also provides the clearest illustration of weakly overlapping bubble structures appear in the sonar image. In the beamformed image, the acoustic response is more spatially diffuse, and the bubble signatures are accompanied by broader spreading of intensity into the surrounding field. After deconvolution, the acoustic response becomes more compact and more sharply localized around the bubble positions indicated by the camera contours. This shows that the deconvolution reduces contamination from surrounding sidelobe intensity and produces a more compact acoustic response, thereby improving the qualitative localization of the bubble-rich region. In this sense, the sparse bubble plume provides a clear qualitative demonstration of the sharpening effect of the deconvolution step.

The same overall behavior is also observed in a denser bubble plume, shown in Figure 7. The beamformed sonar image captures the presence of this plume, but the response is relatively smeared, making it more difficult to distinguish between the real bubble structures and sidelobe interference. In particular, small closely spaced bubbles tend to merge through the beamforming process into a broader continuous plume-like response. After deconvolution, the plume becomes more compact and better defined, showing that the method improves the localization of dense bubble configurations, making it easier to identify plume boundaries.

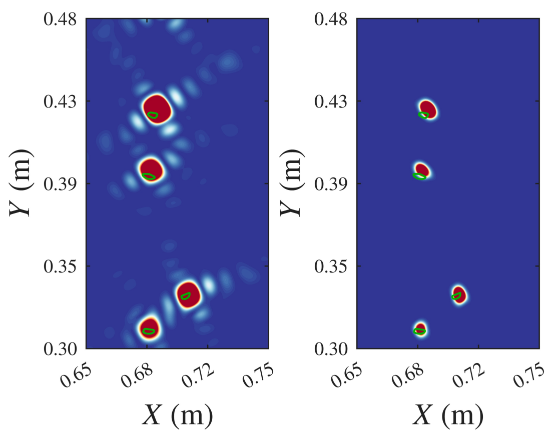

Figure 6: Comparison of sparse bubble plume. The left panel shows the beamformed sonar image, and the right panel the deconvolved image, both with camera-derived bubble contours mapped into sonar coordinates.

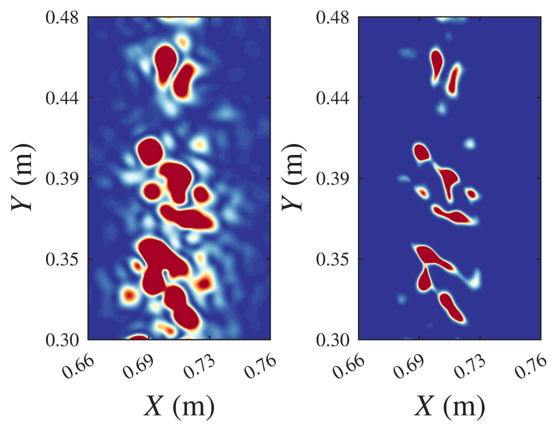

Figure 7: Comparison of dense bubble plume. The left panel shows the beamformed sonar image and the right panel shows the deconvolved sonar image.

CONCLUSION

This study evaluated high-frequency multibeam sonar as a non-intrusive method for characterizing bubble-rich regions relevant for air lubrication flows. Synchronized multibeam sonar and optical measurements were performed in a controlled laboratory setup, and the sonar images were processed using Richardson-Lucy deconvolution with a practical calibrated point spread function parameter, based on calibration-sphere measurements.

The results show that the method can localize bubble plumes and provide meaningful information on plume position, extent and overall structure. For both sparse and dense bubble distribution, the deconvolution method reduced sidelobes and limited the spread of acoustic energy, leading to a more compact sonar response and improved qualitative agreement with the bubble regions observed in the optical images.

The study also highlights an important limitation of the approach. Although the method improves localization, it does not provide reliable quantitative reconstruction of bubble size for targets near the resolution limit of the sonar. Calibration results showed that 5.5 mm and 9 mm spheres could not be accurately distinguished in size at 0.8 m distance, indicating that the sonar data should primarily be used for bubble position, plume extent and relative concentration rather than exact bubble sizing.

Overall the results indicate that high-frequency multibeam sonar combined with deconvolution has potential to be used in air-lubrication research. The effectiveness of air lubrication depends not only on the presence of injected air, but on where that air is located, how it is distributed, and how long it remains in the near-wall region where drag reduction is most effective. In this context, the present results suggest that the method has potential for resolving the spatial structure of air clusters. However, a more complete characterization of air-lubrication flows still requires complementary techniques, and the present study shows that optical imaging remains essential as a reference for bubble size.

REFERENCES

Ceccio, Steven L. 2010 Friction Drag Reduction of External Flows with Bubble and Gas Injection. *Annual Review of Fluid Mechanics* **42** (Volume 42, 2010), 183–203.

Elbing, Brian R., Mäkiharju, Simo, Wiggins, Andrew, Perlin, Marc, Dowling, David R. & Ceccio, Steven L. 2013 On the scaling of air layer drag reduction. *Journal of Fluid Mechanics* **717**, 484–513.

Elbing, Brian R., Winkel, Eric S., Lay, Keary A., Ceccio, Steven L., Dowling, David R. & Perlin, Marc 2008 Bubble-induced skin-friction drag reduction and the abrupt transition to air-layer drag reduction. *Journal of Fluid Mechanics* **612**, 201–236.

Goodman, Joseph W 2005 Introduction to fourier optics. *Introduction to Fourier optics, 3rd ed., by JW Goodman. Englewood, CO: Roberts & Co. Publishers, 2005* **1**.

Huang, Jie, Zhou, Tian, Du, Weidong, Shen, Jiajun & Zhang, Wanyuan 2018 Smart ocean: A new fast deconvolved beamforming algorithm for multibeam sonar. *Sensors* **18** (11).

Kim, Young-Rong & Steen, Sverre 2023 Potential energy savings of air lubrication technology on merchant ships. *International Journal of Naval Architecture and Ocean Engineering* **15**, 100530.

Kitagawa, Atsuhide, Denissenko, Petr & Murai, Yuichi 2019 Behavior of bubbles moving along horizontal flat plates with different surface wettability. *Experimental Thermal and Fluid Science* **104**, 141–152.

Kringel, Christian, Simonsen, Anders Schou, Tziaros, Filotas, Bielicki, Sebastian, Hærvig, Jakob & Papaioannou, Georgios 2025 Experimental study of air lubrication with fluidic oscillators for flat plate drag reduction. *Ocean Engineering* **334**, 121632.

Kumagai, Ichiro, Takahashi, Yoshiaki & Murai, Yuichi 2015 Power-saving device for air bubble generation using a hydrofoil to reduce ship drag: Theory, experiments, and application to ships. *Ocean Engineering* **95**, 183–194.

Li, Jie, Jia, Jiace, Hong, Deyue, Zhu, Yi, Yang, Shuo, Qian, Zhiwen & Zhai, Jingsheng 2025 High-resolution underwater imaging via richardson–lucy deconvolution beamforming with acoustic frequency comb excitation. *Journal of Marine Science and Engineering* **13** (12).

Liu, Xionghou, Fan, Jiahao, Sun, Chao, Yang, Yixin & Zhuo, Jie 2021 High-resolution and low-sidelobe forward-look sonar imaging using deconvolution. *Applied Acoustics* **178**, 107986.

Mäkiharju, Simo A., Lee, In-Ho R., Filip, Grzegorz P., Maki, Kevin J. & Ceccio, Steven L. 2017 The topology of gas jets injected beneath a surface and subject to liquid cross-flow. *Journal of Fluid Mechanics* **818**, 141–183.

Mei, Jidan, Pei, Yuqing, Zakharov, Yuriy, Sun, Dajun & Ma, Chao 2020 Improved underwater acoustic imaging with non-uniform spatial resampling rl deconvolution. *IET Radar, Sonar & Navigation* **14** (11), 1697–1707.

Mizokami, Shuji, Kawakita, Chiharu, Kodan, Youichiro, Takano, Shinichi, Higasa, Seijiro & Shigenaga, Ryosuke 2010 Experimental study of air lubrication method and verification of effects on actual hull by means of sea trial. *Mitsubishi Heavy Industries Technical Review* **47** (3), 41–47.

Murai, Yuichi 2014 Frictional drag reduction by bubble injection. *Experiments in Fluids* **55**.

Murai, Yuichi, Tasaka, Yuji, Nambu, Yuichi, Takeda, Yasushi & Gonzalez A., S. Roberto 2010 Ultrasonic detection of moving interfaces in gas–liquid two-phase flow. *Flow Measurement and Instrumentation* **21** (3), 356–366.

Tanaka, Taiji, Oishi, Yoshihiko, Park, Hyun Jin, Tasaka, Yuji, Murai, Yuichi & Kawakita, Chiharu 2022 Frictional drag reduction caused by bubble injection in a turbulent boundary layer beneath a 36-m-long flat-bottom model ship. *Ocean Engineering* **252**, 111224.

Tanaka, Taiji, Oishi, Yoshihiko, Park, Hyun Jin, Tasaka, Yuji, Murai, Yuichi & Kawakita, Chiharu 2023 Downstream persistence of frictional drag reduction with repetitive bubble injection. *Ocean Engineering* **272**, 113807.

Veloso, M., Greinert, J., Mienert, J. & De Batist, M. 2015 A new methodology for quantifying bubble flow rates in deep water using splitbeam echosounders: Examples from the Arctic offshore NW-Svalbard. *Limnology and Oceanography: Methods* **13** (6), 267–287.

Wang, Jian, Cui, Junhong, Li, Ruo, Li, Haisen & Wang, Jing 2026 High-resolution imaging of multi-beam uniform linear array sonar based on two-stage sparse deconvolution method. *Remote Sensing* **18** (3).

Zhang, Jishen, Gabillet, Céline & Billard, Jean-Yves 2021 Experimental Study of the Bubbly Drag Reduction in the Recovery Region of a Separated Turbulent Boundary Layer. *International Journal of Multiphase Flow* **142**, 103697.

Zhang, Wanyuan, Zhou, Tian, Li, Jianghui & Xu, Chao 2022 An efficient method for detection and quantitation of underwater gas leakage based on a 300-khz multibeam sonar. *Remote Sensing* **14** (17).